SAND2021-3420J

Utilizing Computer Vision and Artificial Intelligence Algorithms to Predict and Design the Mechanical Compression Response of Direct Ink Write 3D Printed Foam Replacement Structures

Devin J. Roach[1,4], Andrew Rohskopf [2], Craig M. Hamel [3],

William D. Reinholtz[4], Robert Bernstein[5], H. Jerry Qi[1*], Adam W. Cook [4*]

[1] The George W. Woodruff School of Mechanical Engineering, Georgia Institute of Technology, Atlanta, 30332 GA, USA

[2] Massachusetts Institute of Technology, Department of Mechanical Engineering, Cambridge, MA 02139, USA

[3] Materials and Failure Modeling, Sandia National Laboratories, 87123 NM, USA

[4] Advanced Materials Laboratory, Sandia National Laboratories, 87123 NM, USA

[5] Organic Materials Science, Sandia National Laboratories, 87123 NM, USA

[*] Corresponding authors HJQ: qih@me.gatech.edu
AWC: acook@sandia.gov

Abstract

Additive Manufacturing (AM) of porous polymeric materials, such as foams, recently became a topic of intensive research due their unique combination of low density, impressive mechanical properties, and stress dissipation capabilities. Conventional methods for fabricating foams rely on complex and stochastic processes, making it challenging to achieve precise architectural control of structured porosity. In contrast, AM provides access to a wide range of printable materials, where precise spatial control over structured porosity can be modulated during the fabrication process enabling the production of foam replacement structures (FRS). Current approaches for designing FRS are based on intuitive understanding of their properties or an extensive number of finite element method (FEM) simulations. These approaches, however, are computationally expensive and time consuming. Therefore, in this work, we present a novel methodology for determining the mechanical compression response of direct ink write (DIW) 3D printed FRS using a simple cross-sectional image. By obtaining measurement data for a relatively small number of samples, an artificial neural network (ANN) was trained, and a computer vision algorithm was used to make inferences about foam compression characteristics from a single cross-sectional image. Finally, a genetic algorithm (GA) was used to solve the inverse design problem, generating the AM printing parameters that an engineer should use to achieve a desired compression response from a DIW printed FRS. The methods developed herein present an avenue for entirely autonomous design and analysis of additively manufactured structures using artificial intelligence.

Keywords: foams; machine learning; genetic algorithm; predictive modelling; computer vision

Graphical Abstract

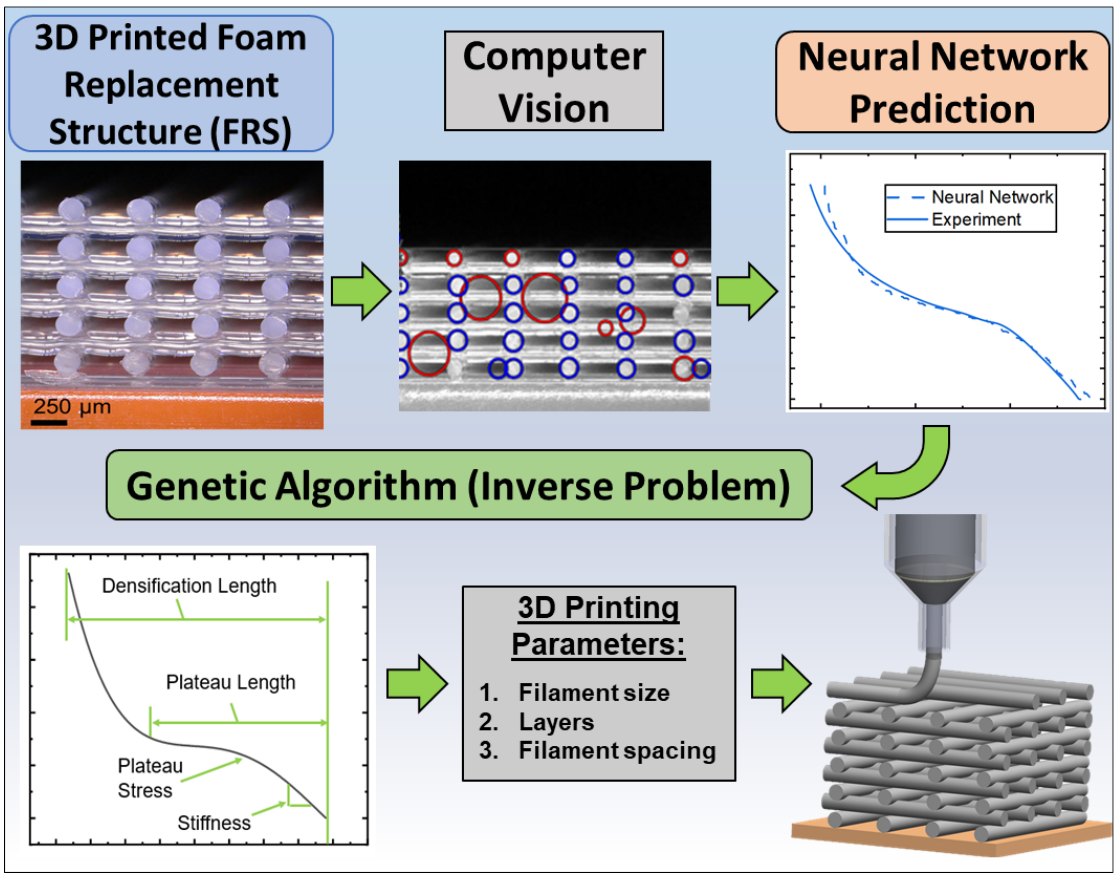

A novel approach was developed to determine the mechanical properties of additively manufactured (AM) foam replacement structures (FRS) using a neural network and computer vision algorithms. Using this methodology, simulation times can be dramatically reduced, allowing for the implementation of a genetic algorithm which can determine the optimal AM parameters to achieve a targeted mechanical compression response.

1. Introduction

Naturally occurring porous materials such as wood, bone, and cork found widespread uses throughout history due to their mechanical robustness despite their light weight. Recently, man-made porous materials, commonly known as foams, became a topic of intensive research with increasing applications in transportation, packaging, insulation [1], sports equipment [2, 3], aerospace [4, 5], and biomedicine [6, 7].

Traditional foams, a type of cellular solid, consist of stochastic arrangements of material and voids which lead to their unique properties [8, 9]. Various methodologies have been utilized for preparing foams including phase separation [10, 11], internal phase emulsion [12, 13], immersion precipitation [14, 15], direct templating[16, 17], and gas foaming [18]. Many of these methods rely on multi-step procedures which typically require high temperatures, pressures, or chemical leeching and result in relatively stochastic nucleation of pores. This can be highly disadvantageous for engineers who wish to gain precise control over the density or mechanical properties of foams for specific applications. Some attempts to generate foams with varying pore densities have been made by adjusting gas pressure, particulate size, or temperature. A notable example for generating more direct control over pore size and relative density is the use of sacrificial materials, such as salt or urea prills, which can be leached out after being placed in water baths [19-21]. These methods, however, are time and process intensive while producing highly ordered foams with precise spatial control and micro-scale features, remains a crucial challenge.

In recent years, additive manufacturing (AM), also known as 3D printing, presented itself as a solution to this problem since complex designs can be rapidly implemented and manufactured with high spacial control without the need for expensive tooling, casting dies, or post-processing [22-24]. Direct-ink write (DIW) 3D printing, in particular, came under special attention due to its ability to process a wide range of materials including elastomers [25-27], ceramics [28, 29], conductive pastes [30-32], hydrogels [33, 34], and other smart materials [35-39]. Due to this wide library of printing materials and precise extrusion process, many efforts have been made to fabricate engineered structures that behave like foams, or foam replacement structures (FRS), using DIW. In 2006 Lewis et. al printed colloidal gels which could span gaps in underlying layers and ultimately produce an FRS with an array of material and voids [35]. Since then, more complex cellular solids,

have been developed to generate FRS with unique strain-energy absorption capabilities or strength-to-weight ratios [5, 40]. Still, the FRS designs presented in these works are highly experience-dependent, relying on unit cell designs intended for specific applications, demonstrating a need for the investigation of tunable foam design strategies which can solve a variety of realistic mechanical loading scenarios.

Multiple design strategies have been employed to further modify the mechanical response of foams by altering the matrix material or pore design. For example, grayscale 3D printing has been introduced allowing mechanical tunability for foam matrix materials [41]. Karyappa, et. al. combined DIW and immersion precipitation to fabricate foams which have widely tunable porosity from micro to nano scales [42]. In addition to adjustments in pore dimensions and matrix material, entire foam architectures may also be altered to produce unique mechanical responses. Duoss et. al. DIW printed two elastomeric foams with slightly differing configurations, however, each exhibited drastically distinct load responses ultimately suggesting the ability to independently tailor mechanical response of cellular solids via micro-architected designs [22]. Apart from intuitive design strategies, finite element method (FEM) simulations have been employed to characterize layers of viscoelastic materials and use them to find optimal designs for energy dissipation in packaging and helmet applications [43]. Many researchers have also attempted to model porous foams directly, though the viscoelastic models are exceedingly nonlinear while microstructural models for highly complex 3D structures are challenging, especially at large deformations[44-46]. The primary drawback of FEM simulations, however, is that they are computationally expensive and exploring a large design space, with many architectures or pore sizes, would be very time intensive. We therefore seek a strategy that can reproduce mechanical characteristics such as compression curves within times on the order of minutes on simple desktop or laptop computers, so that engineers may use such models to explore a large design space. Artificial neural networks (ANNs), a subset of machine learning (ML) methods, are capable of rapidly interpolating to identify trends and patterns within complex data, and therefore serve as an excellent solution to the problem of accurately modelling mechanical characteristics in a computationally cheap and efficient manner.

Due to their ease of implementation, rapid pattern recognition, and ability to make complex decisions, ANNs have found widespread use in search engines, financial modelling, marketing, and self-driving vehicles. Recently, ANNs have been applied to classical mechanics problems such as

predicting the crack propagation characteristics of metals [47], torsion in iron alloys [48], or multi-scale quantum mechanical models [49, 50]. Gu, et. al. utilized ANNs to design fracture resistant composite structures with varying toughness and strength ratios [51]. This approach, however, relies on data gathered from thousands of FEM simulations for 2D architectures, limiting its applicability for directly modeling complex 3D porous micro-structures. Recently, Jordan, et. al. substituted FEM simulations for a small set of experimental results to train an ANN which could describe the temperature and strain rate dependent mechanical response of polypropylene [52]. Here, a relatively small experimental set could be used to train an ANN that accurately represents a complex architectural design space. In creating an ANN model, however, one must provide adequate inputs that describe the situation to be predicted. To increase the usability and convenience of the model, the process of extracting inputs based on simple measurements or calculations should be rapid and automated. In many applications ranging from self-driving vehicles to mechanical property prediction based on material geometry, simple images may contain the information which must be input to the ANN model. The automatic inspection and rapid data acquisition from images for this purpose can be readily achieved using computer vision.

Computer vision has seen rapid advancements in recent years extracting and utilizing critical parameters from images enabling technologies such as self-driving cars, automated health monitoring [53, 54], and facial recognition. The most common use of computer vision in the field of mechanics is for digital image correlation (DIC) which is used to determine the displacement of a structure as a function of time [55-59]. These approaches, however, use computer vision to track pattern displacement over large time intervals and therefore require substantial datasets and complex analysis software, rather than the analysis of simple static images. While these studies demonstrate possible applications of using ML in materials design, they were mostly focused on using ML models to predict properties of materials or structures rather than designing new structures with desired properties. To design a foam to have specific mechanical behavior, the design problem must be framed as an optimization problem to find the optimal design parameters.

A genetic algorithm (GA) is a multi-objective optimization technique which mimics the process of natural selection to achieve optimal design solutions based on a desired outcome. Consequently, GAs have demonstrated great promise in rapidly discovering optimized solutions for complex design problems in chemistry[60], electromagnetics[61], molecular modelling[62],

composite design[63], 4D printing [64, 65], and a variety of other engineering disciplines [66, 67]. Regarding the mechanics of composites, training an ANN can often become computationally unfeasible due to the large mesh densities and representative volume element (RVE) sizes required to achieve a size converged piece of training data for the GA to utilize. For this reason, researchers have turned to GAs for determining optimal composite designs for critical aerospace components [68], prosthetics [69], lattice structures [70, 71], among other exciting applications.

In this work, we develop a novel methodology for approaching both the mechanical analysis and the design of DIW printed FRS using a combination of ANN, computer vision, and GA. An ANN is utilized to predict the mechanical compression characteristics of printed FRS. By using computer vision algorithms, static cross-sectional images of experimental specimens could provide adequate ANN inputs describing the FRS printing parameters. The advantage of rapidly obtaining compression characteristics based on printing parameters allowed us to implement a GA, rapidly solving optimization problems in a complex design space. As a result, the GA could tackle the inverse problem of obtaining ANN inputs, or FRS printing parameters, to yield a desired mechanical compression response.

We begin this study in Section 3.1 by DIW printing an array of FRS with various thicknesses, filament spacing, and filament diameters. After compression testing, general trends within the data can be identified as the printing parameters are adjusted, however, capturing the complex relationship between each of the variables is tedious. In Section 3.2, a computer vision algorithm is produced which can determine foam printing parameters from a cross-sectional image with a small error. Section 3.3 presents the implementation of an ANN that will be trained using the experimental data developed in Section 3.1. The ANN can then be used to not only accurately predict the compression behavior of a foam using its cross-sectional image but can also be employed to infer the compression data of foams for which we have no prior mechanical data. Lastly, in Section 3.4, a GA is developed which solves the engineering design problem of finding printing parameters, i.e. ANN inputs, to obtain a desired compression curve. This methodology demonstrates the great potential for motivating the design of additively manufactured structures that cannot be driven by mechanical models due to their complexity, time of implementation, or nonexistence.

2. Materials and Methods

2.1 Materials

2.1.1 SE 1700

The material used in this study was a two-part silicone elastomer, DOWSIL SE 1700, produced by DOW Chemical (Midland, MI, USA). The silicone ink was prepared for printing by homogenizing at a ratio of 10:1 part A:B in a vacuum planetary mixer (Think ARV 310, Thinky Inc., Laguna Hills, CA, USA) for 60 s at 2000 rpm and 7 kpa. Following mixing, the silicone resin was transferred to 60 mL syringes and centrifuged at 2000 rpm for 3 minutes prior to printing. The rheological properties of SE 1700 and the suitability of its use with DIW printing techniques did not require characterization beyond what has been previously reported [22].

2.2 Printing and Characterization Methods

2.2.1 Direct ink write (DIW)

A custom engineered deposition system having computer-controlled motion stages was used to translate a build platen in the X-Y plane. A constant displacement syringe pump affixed to the translating motion stage of the Z-axis provided a method of depositing silicone at known volumetric dispense rates. Custom toolpath generation software was used to coordinate the movement of the XYZ motion stages and material extrusion pump to fabricate FRS from predefined toolpaths. Key design variables and printing conditions of the FRS are presented in Table 1. The silicone elastomer was printed at room temperature onto aluminum plates pretreated with a PTFE mold release agent. After printing, the FRS was transferred to an oven and cured for 30 minutes at 150°C, followed by 24 hours at 125°C.

Table 1: Critical FRS design and printing parameters. For each nozzle size used to print FRS, the number of printed layers was incremented by 5 layers up to the maximum number of layers shown. The spacing between filaments was incremented by integer multiples of the nozzle diameter. In total, 250 unique FRS were printed.

Nozzle Diameter (mm)	Extrusion Rate (cm^3/min)	Layer Hight (mm)	Number of layers	Filament Spacing (x's nozzle diameter)	Printing Speed (mm/s)	Number of unique FRS

0.250	0.0972	0.2150	5-60	1-10	40	120
0.410	0.2543	0.3526	5-40	1-10	40	80
0.584	0.4701	0.5022	5-25	1-10	40	50

2.2.2 Compression testing

To obtain the compression data for the FRS, a simple compression test was performed using an Instron (Norwood, MA, USA) 5564 Universal Testing Machine. During testing, samples were centered on the bottom stationary platen (platen size, 6 inches diameter). The indenter or "ram" (moving platen) had a diameter of 1.125 inches. Both platens were made of polished stainless steel. The platens were cleaned and inspected to ensure that they were free of dust or broken particles from previous experiments. The compression rate was 0.2 mm/s. To characterize the mechanical compression response of the FRS, the nominal stress and compression gap were measured. The nominal stress is defined as the measured force divided by the area of the FRS's 2D footprint. The compression gap is defined as the gap between the two platens. In this work, only the first compression loading cycle was observed as subsequent compression cycles lead to different mechanical compression responses [72]. The first three compression cycles for FRS 51-53 were plotted and can be seen in Figure S1 in the Supplementary Information (SI).

2.2.3 Imaging of foams

Cross-sectional images of the FRS were obtained using an optical microscope (Keyence VHX 5000). A scale bar was superimposed on each image to be later read by the computer vision algorithm developed in this study. Sample cross-section images can be seen in Figure S2 in the SI.

2.3 Machine Learning Methods

The computer vision, neural network, and genetic algorithm were written using Matlab R2020a (MathWorks Inc., Natick, MA, USA). Special toolboxes were installed to perform certain actions. To perform the computer vision tasks, the Computer Vision toolbox was installed. The training and execution of the ANN relied on the Statistics and Machine Learning, GPU coder, Parallel Computing, Deep Learning, and MATLAB Compiler SDK Toolboxes.

3. Results & Discussion

3.1 DIW of FRS

The use of DIW printing provides the advantage of printing complex architectures with precise dimensional accuracy and can therefore be used to print structures that perform like foams. In this study the silicone elastomer was DIW printed on a flat substrate to produce a wide variety of FRS structures with simple cubic architectures. A schematic of the DIW printing process utilized to produce the FRS can be seen in Figure 1a. The inset of Figure 1a shows each of the FRS design parameters that will be modulated during this study, namely the filament diameter, filament spacing, and number of layers. An image of a DIW printed FRS is shown in Figure 1b. Figures 1c and 1d are graphical depictions of the entire design space that will be focused on in this study. As seen in Figure 1c, three different filament diameters were used while the number of layers was adjusted linearly, in intervals of five, for each. Finally, Figure 1d shows that for every layer height, ten filament spacings were printed. Modulating the DIW design parameters in this manner led to 250 unique printed FRS designs. Tabulated values for each of the printing parameter combinations used and the associated foam numbers are listed in Table S1 in the SI.

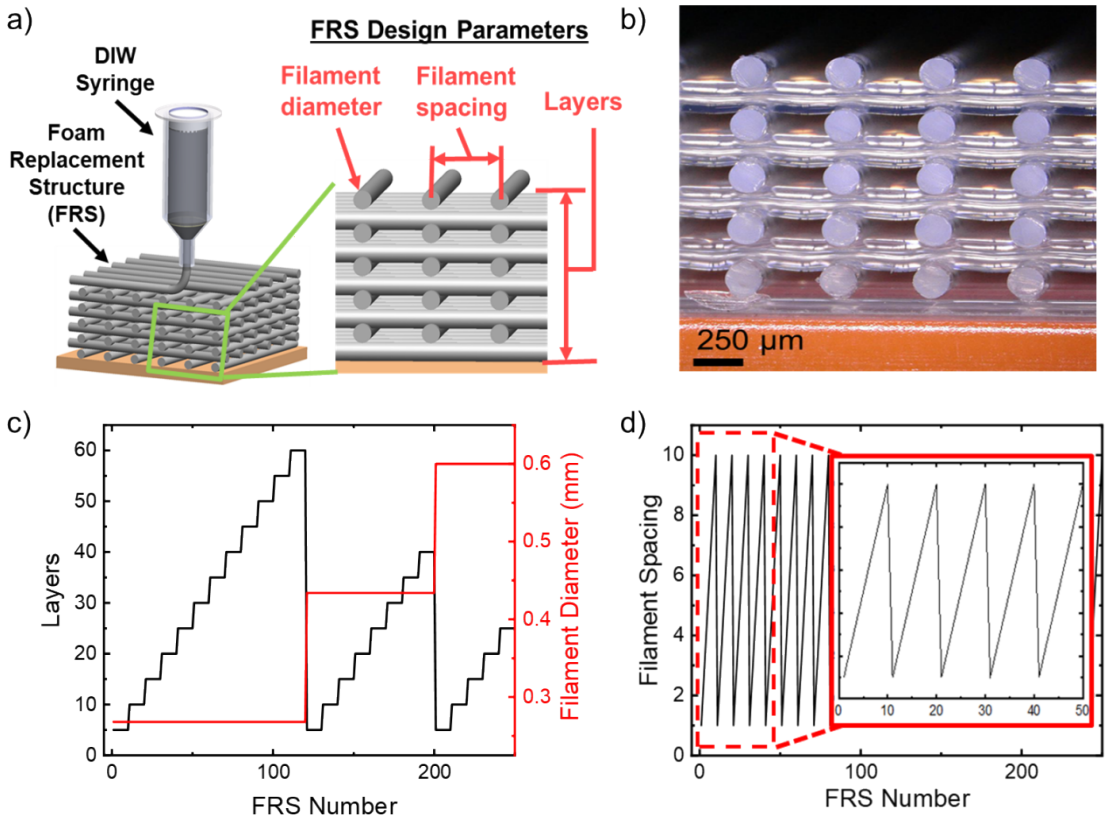

Figure 1: FRS printing parameters and experimental design space. a) Schematic of FRS being DIW printed with the inset highlighting the three primary design parameters adjusted throughout the study: namely, filament diameter, filament spacing, and number of layers. b) Photograph of a DIW printed FRS. c) Graph depicting the filament diameter and number of layers design space for the 250 printed FRS used in this study. d) Graph showing the filament spacing variable as a function of the printed FRS number with the inset demonstrating that the spacing was changed for each foam in the design space.

3.1.1 Compression results

Following AM of the silicone FRS, their performance was evaluated through analysis of mechanical compression results. It is important to note that we observed the nominal stress as a function of the FRS compression gap as it provides a direct mapping of printed FRS performance in 1D compression behavior to end-use applications. A further discussion regarding the use of this method for more general loading scenarios can be found in Section 4. The general trends and results are shown below in Figure 2. Figure 2a shows the compression results for FRS 91 through FRS 97 which have the same filament diameter and number of layers (0.250 μm and 50, respectively) but have different filament spacings. This graph demonstrates that by increasing the filament spacing while fixing the other two printing parameters, the FRS trend from stiff to soft. This is consistent with typical foam mechanics where higher relatively density leads to higher stiffness. Alternatively, Figure 2b shows that by increasing the number of layers, while fixing the filament diameter and spacing (0.250 μm and 5, respectively), the FRS have similar plateau stresses but differing plateau lengths.

Some interesting observations can be made about the FRS characteristics when a derivative of the nominal stress with respect to the compression gap is plotted. The results for FRS 51 through FRS 57 are plotted in Figure 2c and two critical points are highlighted with roman numerals. Roman numeral (I) indicates where the foam transitions from its initial, linear-elastic response to the buckling plateau region. In this region, the stress remains relatively constant despite an increased deformation. This is caused by a buckling response of the FRS causing it to become softer. Roman numeral (II) indicates a second change in the slope of the compression curve where the FRS enters densification. This occurs when the pore walls begin to come into contact with

each other making the FRS behave like a solid polymer resulting in the FRS becoming asymptotically stiff. A photograph of a FRS at each of these points can be seen in Figure 2d. The relative location of these points can be used as critical design parameters for engineers when deciding how to construct their foams for specific applications.

It may be possible to capture the general trend observed in these figures using a complicated power law relationship between the printing parameters and compression results. However, when multiple variables are adjusted, it will be become increasingly complicated to draw relationships with their resulting mechanical compression properties. Therefore, it is imperative to capture the trend using a more complicated model, however, microstructural FEM simulations tend to be computationally expensive, especially for large displacements where elements contact or become inverted. Therefore, using the data recorded in this section, an artificial neural network (ANN) was trained to capture the complex relationship between the printing parameters and resulting mechanical response.

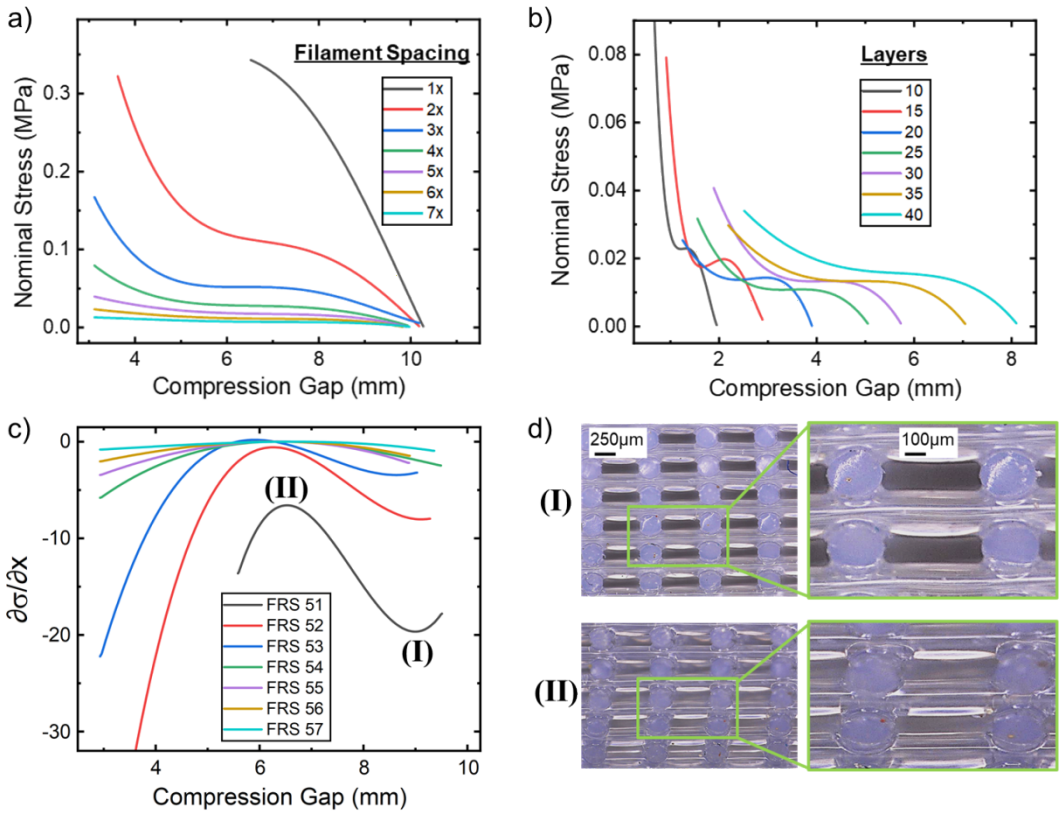

Figure 2: Compression characteristics of various DIW printed FRS, or foams. a) Compression curves for foams that have varying filament spacings demonstrating a trend from stiff to soft with

increasing filament spacing. b) Compression curves for FRS that have varying layer heights demonstrating differing plateau stresses but highly differing plateau lengths. c) Derivative of the compression curve with roman numerals (I) and (II) indicating the critical points during the compression of an FRS. d) Images of an FRS at each of the points indicated by roman numerals in Figure 2c indicating when an FRS begins to buckle (I) and densify (II).

3.2 Computer vision

Computer vision tools have seen large advancements in recent years enabling rapid identification of critical features from images. Cross-sectional images of the DIW printed FRS were taken and a computer vision algorithm was written to determine the filament diameter, filament spacing, and number of layers. Figure 3a shows a cross-sectional image of an FRS with labels of each of the parameters being mined. The following section details the design, results, and accuracy of the computer vision algorithm using the methods outlined in the reference [73] where sigmoidal functions were observed.

To determine the relevant information from the cross-sectional images, novel methods and various pre-built algorithms were combined. To find the filament diameter, the Sobel and Canny edge finding algorithms were implemented. More information on these methods can be found in Sharifi, et. al. [74]. Based on the detected edges, object polarization was used to find the circles as their color differed greatly compared to the surrounding regions. In some cases, additional circles were found by the algorithm and omitted using a 5% outliers filter. Figure 3b shows an example of the kept and omitted circles highlighted with blue and red, respectively. To validate the algorithm, the resulting accuracy of each edge detection method is depicted graphically in Figure 3c. Here, the error between the filament diameter detected by the computer vision algorithm and the measured filament diameter were calculated and plotted with their relative frequency. From this data it was determined that the Canny edge finding method determined the filament diameter with a higher accuracy and would be used for the remainder of the study.

To find the number of layers of an FRS, the Canny edge detection method was used, followed by the Hough line finding algorithm [75]. Figure 3d shows the lines detected using this method, as indicated by green lines overlaid on the image. By identifying the top and bottom lines, subtracting the distance between them in the y direction, and dividing by the filament diameter (as

determined by the computer vision algorithm), an estimation of the number of layers could be made. Figure 3e shows that the number of layers found using this method closely matches the number of printed layers. Lastly, the spacing between the filaments was determined by subtracting the distance between centroids of the circles found in Figure 3b in the x-direction. Figure 3f shows the error using this approach follows a zero-centered Gaussian curve and therefore is highly accurate.

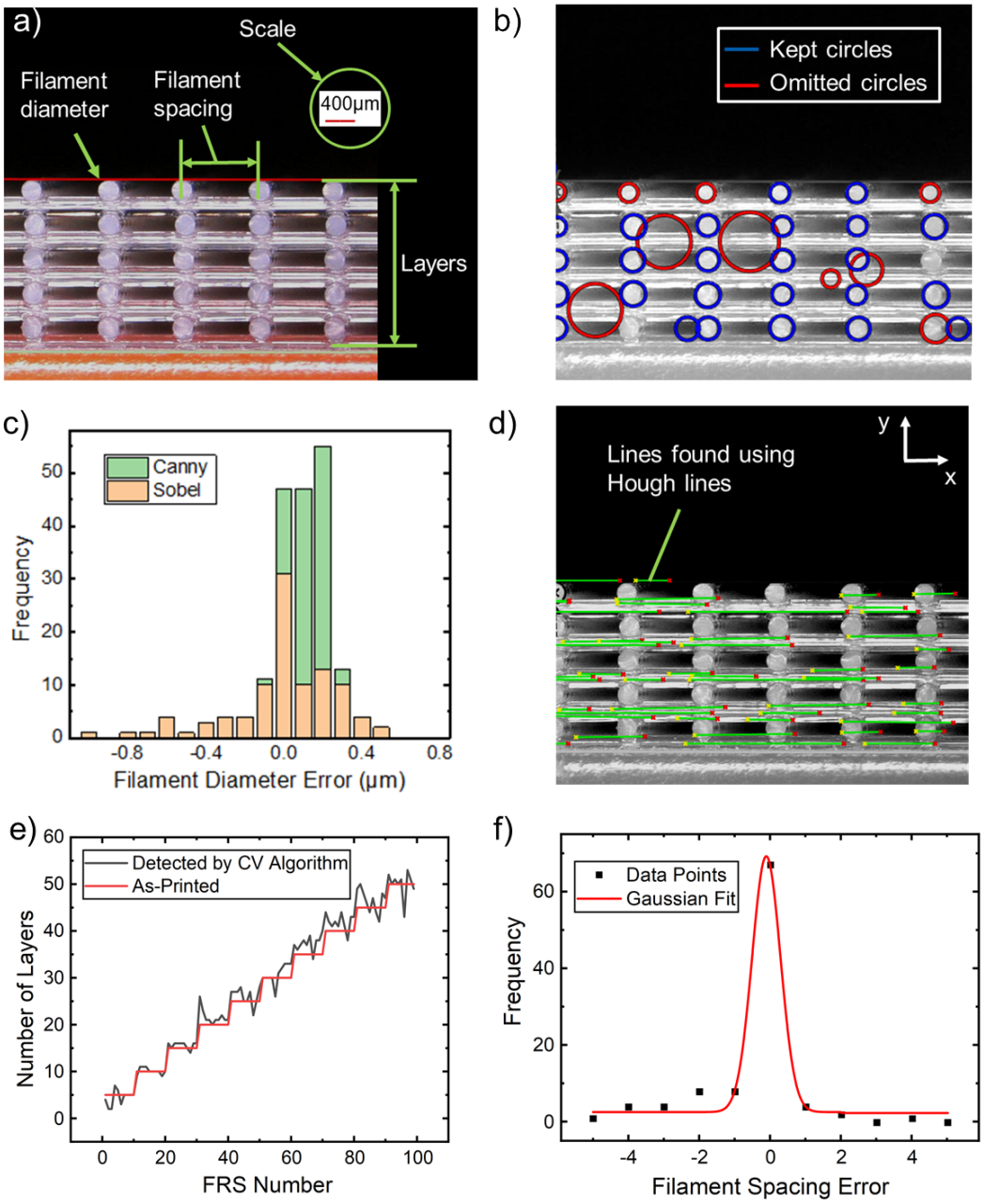

Figure 3: Results of the computer vision algorithm. a) Sample cross-sectional image fed to the computer vision algorithm which was used to determine the primary FRS printing parameters

labeled in the image. b) Circles found using the computer vision algorithm with the blue circles being kept and the red being omitted using an outlier approach. c) Relative frequency of filament diameter error when using the Canny and Sobel edge finding techniques. d) Lines found using the Hough lines finding technique for determining the number of layers. e) Comparison between the number of layers detected by the computer vision algorithm vs. the number of printed layers for the first 100 FRS. f) Frequency of error values for the filament spacing as determined by the computer vision algorithm demonstrating a high frequency of zero error.

3.3 Artificial Neural Network

When engineers design foams, they need to understand how they will act in the context of their desired applications. However, complex architectural geometry, large elastic deformations, rate dependencies, and temperature dependencies make it extremely difficult to precisely model the mechanical compression response of foams. Therefore, a model which can accurately predict foam behaviors for a large design space, using a relatively small experimental set is required. ANNs are a class of machine learning algorithms that can be used to rapidly parameterize a design space. ANNs are comprised of a collection of interconnected nodes, sometimes called neurons. ANNs aggregate neurons into multiple layers which create mathematical relationships between inputs and outputs based on a set of training data. For further information and terminology surrounding ANNs please refer to Hecht-Nielson, et. al. [76]. Here, an ANN was trained using the mechanical compression results of the printed FRS studied in Section 3.1 and was able to successfully parameterize a complex architectural design space for large deformations.

3.3.1 Design of the neural network

The ANN used in this study is a shallow neural network with an input layer of 3 nodes, a single hidden layer with 500 nodes, and an output layer of 400 nodes as shown schematically in Figure 4a. The inputs to the ANN are the three printing parameters: filament diameter, filament spacing, and number of layers. The outputs are 200 x points and 200 y points which form a single compression curve. The ANN was trained using backpropagation and a mean square error (MSE) was utilized to rate the error at various epochs, or iterations. The training set was made up of the experimental compression data gathered from the 250 printed FRS as described in Section 3.1. The data was

split into 80% training, 10% validation, and 10% testing data to properly interrogate the accuracy of the ANN. The ANN was determined to be sufficiently trained when the MSE reached a value of 0.1. Training the ANN took 67 seconds in a total of 2870 epochs, or iterations. For further information about the training of the ANN and its accuracy in recreating the relationship between the FRS printing parameters and compression curves please see Section S4 in the SI.

3.3.2 Predictions using neural network

The ANN described above can accurately predict the compression response of AM foams given their printing parameters. Figure 4b shows a comparison between the compression response recording during experiments and the response generated by the ANN. It is important to note that the compression curves used in Figure 4b were not used in the training set. In addition to accurately predicting the compression behavior of FRS within the design space of the ANN, the network can also make inferences about FRS within gaps in the design space. Figure 4c shows the ANN-predicted compression curve for a hypothetical FRS with printing parameters between those of Foams 81 and 92. Here, both the filament spacing and the number of layers were adjusted to design parameters that were not used to train the ANN. The ANN accurately predicted a compression curve for 2.5 filament spacings and 48 layers, demonstrating its ability to make accurate inferences about FRS that are within the design space for which the ANN has no prior data. To validate this prediction, the FRS was printed, and its resulting compression curve, as determined by experiment, demonstrates good agreement with the ANN prediction as seen in Figure 4c.

Due to the advantages garnered by the computer vision and ANN algorithms, they could be combined to generate mechanical compression data using a simple cross-sectional image of a printed FRS. A demonstrative example is shown in Figure 4d. Here, the computer vision algorithm determines the DIW printing parameters using a cross-sectional image of Foam 22. Then, using these parameters as inputs, the ANN can accurately (within 4.1% mean error) predict the FRS's resulting mechanical compression response. This entire process takes less than a few seconds of computational time.

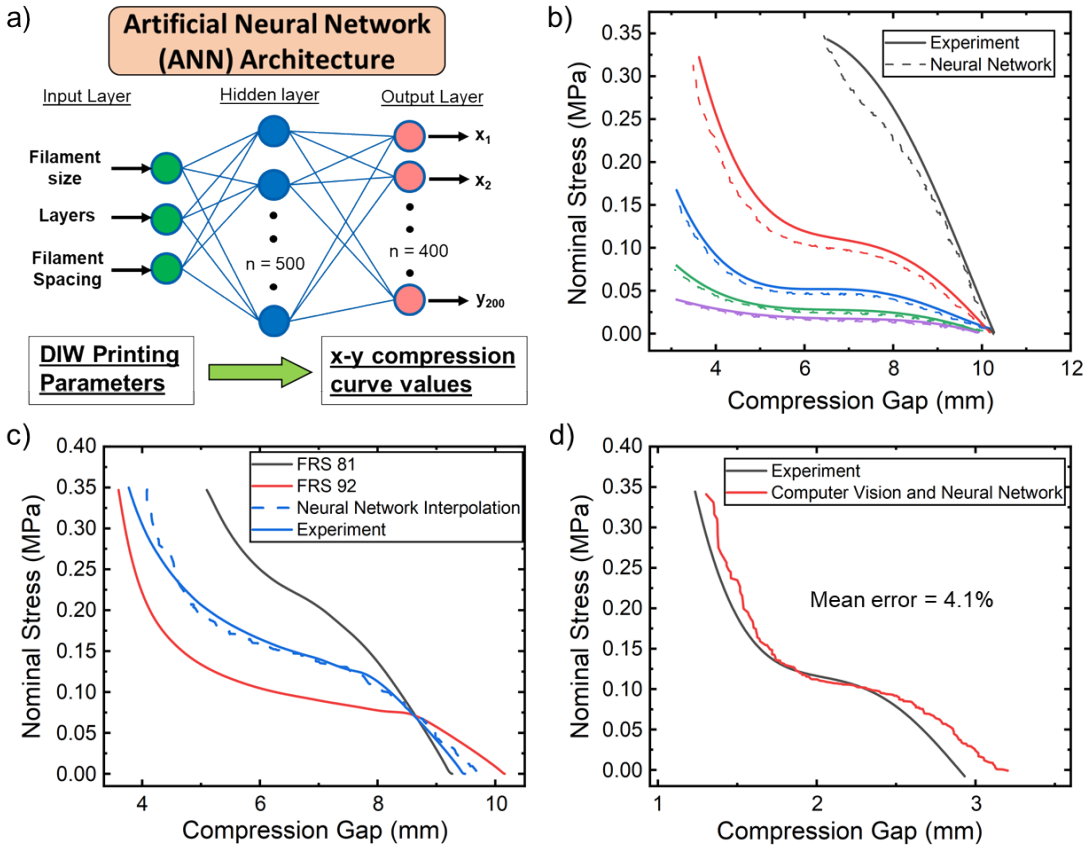

Figure 4: Results using the artificial neural network (ANN). a) Schematic of the ANN architecture consisting of the three layers used to predict the relationship between the DIW printing parameters and the FRS's mechanical compression curve. b) The neural network can be used to accurately predict the compression data from experiments that were not included in training data. c) The neural network can accurately make inferences about FRS that are within gaps in the design space. d) By combining the neural network and computer vision algorithms, an FRS's mechanical compression response could be accurately predicted using a cross-sectional image.

3.4 Genetic Algorithm for FRS Design

The results outlined in Section 3.3 can be used to rapidly model FRS from a large architectural design space, even up to large deformations. The advantages garnered by this approach allow engineers to rapidly characterize foams, however, searching an extremely large design space for an optimized FRS design based on specific mechanical constraints may remain a challenge. This problem can be solved by employing another AI-based solution, called a GA, which can rapidly search the design space to find optimized solutions based on target parameters. Figure 5a shows

the four compression parameters that an engineer would use when designing an FRS, namely, stiffness, plateau stress, plateau length, and densification length.

A flow chart detailing the GA-based design process can be seen in Figure 5b. By inputting the four target compression parameters, the GA will output the FRS printing parameters needed to produce the desired mechanical compression response. The gray section of Figure 5b represents the GA. First, the target compression parameters are used to generate a target compression curve which will be used as the goal of the GA-optimization algorithm. The GA begins by creating an initial population, or first generation, of randomly generated printing parameters within the design space. Next, the ANN developed in Section 3.3 generates compression curves based on the first generation of printing parameters. To determine if the generated compression curves match the target compression curve a fitness function is utilized for optimization. The expression used to determine the fitness of the compression curve for the 200 y-values is as follows,

$$\mathcal{F}_y = \frac{1}{200}\sum_{i=1}^{200}\sqrt{\left(y_i^{target} - y_i^{actual}\right)^2} \tag{1}$$

where y_i^{target} is the y point on the target compression curve, y_i^{actual} is the y point generated by the ANN [64]. The fitness for the x values, $\mathcal{F}_x$, is also calculated in this way. $\mathcal{F}_x$ and $\mathcal{F}_y$ are then normalized between 0 and 1 such that an overall fitness function can be expressed as follows,

$$\mathcal{F} = \mathcal{F}_{norm,x} + \mathcal{F}_{norm,y} \tag{2}$$

Here, the goal is to minimize the error between the target x-y values and the ANN-generated x-y values, which can be expressed as

$$\min_{xy^{actual}} \mathcal{F} \ , \tag{3}$$

for each generation, or iteration of the GA. If an optimized solution is not found the next generation of ANN input parameters is developed by keeping the best solutions from the previous generation and performing mutation and crossover operations to the remainder of the population. For more details on how this process works the readers are referred to Coley, et. al. [66].

To test the viability of the GA for solving a foam design problem, a target compression curve was developed based on four critical foam design parameters. In this example, the densification length, plateau length, plateau stress, and stiffness were set to 9mm, 6mm, 0.125 MPa, and 0.4, respectively. Figure 5c shows the fitness of a population of printing parameters as a function of

the generation, or iterations through the GA. It was observed that 20 individuals in a single population could achieve the best fitness and fastest convergence. The target and achieved compression curves can be seen in Figure 5d with the inset shows the resulting 3D printing parameters determined by the GA to produce an FRS with the desired compression curve. Lastly, Figure 5e shows that the GA-based design approach may not always produce unique solutions. Here, two 3D printing parameter design solutions were discovered, greatly increasing a designer's potential for achieving a desired response. These results demonstrate great promise for engineers seeking to design foams with specific mechanical characteristics in both a time and computationally efficient manner.

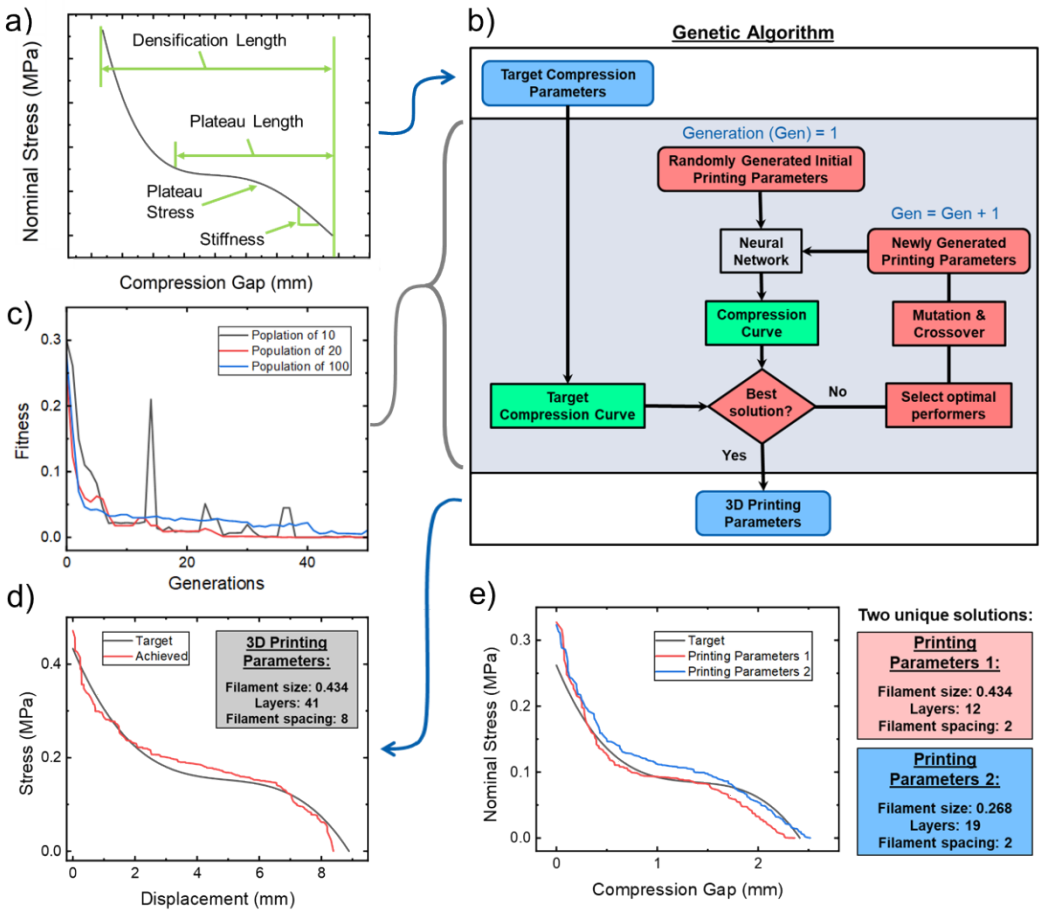

Figure 5: Using a genetic algorithm (GA) to design foams based on target mechanical properties. a) The four mechanical compression parameters input into the GA to construct a target compression response for a foam. b) Flowchart detailing the components of the genetic algorithm used to determine the optimal FRS printing parameters based on target compression parameters. c)

Convergence statistics for the GA for three different population sizes. d) The resulting 3D printing parameters determined by the GA to achieve the target compression curve. e) The GA can also determine multiple 3D printing parameter solutions for a single target compression curve.

3.5. Discussion

This work presents an avenue for dramatically reducing computational and experimental costs by implementing AI-based approaches in the mechanical characterization and design of AM components. While this study focuses on the mechanical compression response of an elastomer-based FRS, this method can be extended to include other materials such as metals, ceramics, or other polymers. Furthermore, other mechanical loading scenarios such as tension or shear can be observed and utilized to train the ANN. The primary implications of this work are three-fold, and each are discussed individually below.

First, we demonstrate that the use of computer vision algorithms can provide real-time, vision-based inspection technique for AM components. This approach can be especially well-suited for high production volume AM environments where each printed object cannot be inspected for its mechanical readiness prior to use. This methodology can be extended to include estimations of the mechanical properties of multi-material AM composites where building constitutive models may not be feasible.

Next, this work demonstrates that ANNs can provide a ready alternative for providing mechanical models when traditional methods such as FEM and continuum mechanical models fall short. For the case of foams, it is very difficult to accurately capture large deformations using FEM models due to element inversions. Therefore, in this study we replace the entire simulation process using a trained ANN. Furthermore, to discover new constitutive laws, experimental data and AI can be used to fill gaps in continuum mechanical models. This approach is called a data-continuum hybrid approach. Using this approach, material laws are substituted for constitutive relationships derived from the ANN. As a notable example, Jordan, et. al. utilized an experimental data set to train a neural network to discover the hardening law for polypropylene up to 60% strain. When combined with existing viscoelastic models, constitutive equations were developed which accurately estimated the polypropylene stress evolution for all strain and temperature histories [52].

While constitutive models describing soft material systems remain a challenge, utilizing data-driven and AI-based predictive modeling can provide a ready solution.

Lastly, we demonstrate that predictive algorithms, such as ANNs, are extremely applicable for rapidly and efficiently providing data for computationally heavy optimization algorithms, such as GAs, which must explore large parameter spaces. Using traditional simulation techniques, such as FEM, to provide inputs to a GA can be time or computationally prohibitive, requiring multiple hours or even days to find a solution. In this paper, by employing an ANN as the de-facto simulation methodology, a large printing parameter design space was rapidly searched, and an optimal solution was found in about one minute of computation time.

Apart from the primary implications of this work, there are some drawbacks and areas where further investigation is required. First, this study only considers one loading type, namely, 1D compression. Many foams and FRS are subject to more complex 3D loading scenarios such as shearing or off-angle compression. Further, different displacement rates were not investigated. To achieve this, more experimental data and a full-field loading experiment would need to be performed and input into the ANN. Therefore, the approach presented here is not a general framework for 3D loading scenarios. Another drawback of this approach is that ANNs are very good at interpolation within large dimensional spaces and with sufficient training data, but typically suffer very poor performance when attempting data extrapolation. Therefore, if the training data does not fully capture the mechanical response of a foam, the ANN will not be able to accurately predict its behavior. The computer vision software presented herein was developed for the specific FRS images gathered in the lab. The image contrast, color scheme, and general shape of critical FRS parameters were well-known, which is not always the case when attempting to image foams or other AM-based structures. Therefore, to develop a more robust computer vision software, further image filtering, processing, and parameter searching techniques should be included.

Finally, to augment the limitations presented above, we propose parallel avenues of future work. First, the use of in-situ characterization methods to inspect AM feedstocks at the time of printing will be developed. This will ensure that the chemical compositions of resins used to print FRS geometries or other AM hardware is considered and well understood at the time of fabrication. Furthermore, the computer vision software can be extended to determine if the FRS being observed matches the printing parameters outlined by the toolpath generation software. This may be

achieved through acquiring additional images of a printed structure and observing key geometrical parameters during or after printing. Using this modified approach, it may be possible to directly extract FRS porosity which could be used as ANN inputs or as machine tool closed loop control parameters. Lastly, incorporation of additional physical parameters to the ANN such as material modulus, coefficient of thermal expansion, and elongation at break will be pursued. This will improve the utility of the method we present while enabling links to physics-based modeling of FRS which may have or require varying material properties.

4. Conclusion

In summary, we presented a novel, AI-based approach for determining the compression behavior of DIW printed foam replacement structures (FRS) using simple cross-sectional images. By recording experimental data for a relatively small number of samples, computer vision and ANN algorithms were utilized to make inferences about an FRS's mechanical compression response. Using this approach, engineers can rapidly make predictions about a foam's mechanical properties and their applicability for specific applications without the need for extensive experimentation or computational modelling. Finally, using the ANN for simulation results, a GA was developed which could rapidly (~60s) discover the optimal DIW printing parameters to produce FRS for target mechanical compression responses. We have therefore demonstrated an AI-based framework for predicting compression characteristics and, using this method, a time and computationally efficient method for designing 3D structures for specific engineering applications.

Acknowledgements

Sandia National Laboratories is a multimission laboratory managed and operated by National Technology & Engineering Solutions of Sandia, LLC, a wholly owned subsidiary of Honeywell International Inc., for the U.S. Department of Energy's National Nuclear Security Administration under contract DE-NA0003525. The authors would like to thank John L. Schroeder and Madison T. Hochrein for their assistance with experimental operations as well as Joshua K. Yee and Chu-Yeu Peter Yang for providing programmatic support. This paper describes objective technical

results and analysis. Any subjective views or opinions that might be expressed in the paper do not necessarily represent the views of the U.S. Department of Energy or the United States Government.

References

1. Mimini, V., et al., *Lignin-based foams as insulation materials: a review.* Holzforschung, 2019. **73**(1): p. 117.
2. Bliven, E., et al., *Evaluation of a novel bicycle helmet concept in oblique impact testing.* Accident Analysis & Prevention, 2019. **124**: p. 58-65.
3. Tumbleston, J.R., et al., *Continuous liquid interface production of 3D objects.* Science, 2015. **347**(6228): p. 1349-1352.
4. Arunkumar, M., et al., *Sound transmission loss characteristics of sandwich aircraft panels: Influence of nature of core.* Journal of Sandwich Structures & Materials, 2017. **19**(1): p. 26-48.
5. Moon, S.K., et al., *Application of 3D printing technology for designing light-weight unmanned aerial vehicle wing structures.* International Journal of Precision Engineering and Manufacturing-Green Technology, 2014. **1**(3): p. 223-228.
6. Ghosh, S., et al., *Direct-Write Assembly of Microperiodic Silk Fibroin Scaffolds for Tissue Engineering Applications.* Advanced Functional Materials, 2008. **18**(13): p. 1883-1889.
7. Michna, S., W. Wu, and J.A. Lewis, *Concentrated hydroxyapatite inks for direct-write assembly of 3-D periodic scaffolds.* Biomaterials, 2005. **26**(28): p. 5632-5639.
8. Gibson, L.J. and M.F. Ashby, *Cellular solids: structure and properties*. 1999: Cambridge university press.
9. Ashby, M.F., *The properties of foams and lattices.* Philosophical Transactions of the Royal Society A: Mathematical, Physical and Engineering Sciences, 2006. **364**(1838): p. 15-30.
10. Mannella, G.A., et al., *Preparation of polymeric foams with a pore size gradient via Thermally Induced Phase Separation (TIPS).* Materials Letters, 2015. **160**: p. 31-33.
11. Hwa, C.C.L.M., D.W., *Method for leaching a polyurethane foam*. 1964.
12. Li, W., et al., *Porous heterogeneous organic photocatalyst prepared by HIPE polymerization for oxidation of sulfides under visible light.* Journal of Materials Chemistry, 2012. **22**(34): p. 17445-17448.
13. Sušec, M., et al., *Hierarchically porous materials from layer-by-layer photopolymerization of high internal phase emulsions.* Macromol Rapid Commun, 2013. **34**(11): p. 938-43.
14. Cheng, L.-P., et al., *Formation of particulate microporous poly(vinylidene fluoride) membranes by isothermal immersion precipitation from the 1-octanol/dimethylformamide/poly(vinylidene fluoride) system.* Polymer, 1999. **40**(9): p. 2395-2403.
15. Wu, C., et al., *Development of biodegradable porous starch foam for improving oral delivery of poorly water soluble drugs.* International Journal of Pharmaceutics, 2011. **403**(1): p. 162-169.
16. Hou, Q., D.W. Grijpma, and J. Feijen, *Porous polymeric structures for tissue engineering prepared by a coagulation, compression moulding and salt leaching technique.* Biomaterials, 2003. **24**(11): p. 1937-47.
17. Yan, X., et al., *Preparation of porous polymer membranes using nano- or micro-pillar arrays as templates.* Polymer, 2004. **45**(25): p. 8469-8474.
18. Salerno, A., et al., *Design of porous polymeric scaffolds by gas foaming of heterogeneous blends.* J Mater Sci Mater Med, 2009. **20**(10): p. 2043-51.
19. Hammetter, C., et al., *Modeling the Behavior of Cellular Silicone Pads in the Structure-*

Continuum Transition. 2014, Sandia National Lab.(SNL-NM), Albuquerque, NM (United States).

20. Gladysz, G.M.C., K.K., *Composite Foams*, in *Encyclopedia of Polymer Science and Technology*. 2004.
21. Mu, X., et al., *Porous polymeric materials by 3D printing of photocurable resin.* Materials Horizons, 2017. **4**(3): p. 442-449.
22. Duoss, E.B., et al., *Three-Dimensional Printing of Elastomeric, Cellular Architectures with Negative Stiffness.* Advanced Functional Materials, 2014. **24**(31): p. 4905-4913.
23. Montgomery, S.M., et al., *Recent advances in additive manufacturing of active mechanical metamaterials.* Current Opinion in Solid State and Materials Science, 2020. **24**(5): p. 100869.
24. Williams, C.B., J.K. Cochran, and D.W. Rosen, *Additive manufacturing of metallic cellular materials via three-dimensional printing.* The International Journal of Advanced Manufacturing Technology, 2011. **53**(1): p. 231-239.
25. Roach, D.J., et al., *Novel ink for ambient condition printing of liquid crystal elastomers for 4D printing.* Smart Materials and Structures, 2018. **27**(12): p. 125011.
26. Roach, D.J., et al., *Long Liquid Crystal Elastomer Fibers with Large Reversible Actuation Strains for Smart Textiles and Artificial Muscles.* ACS Applied Materials & Interfaces, 2019. **11**(21): p. 19514-19521.
27. Kuang, X., et al., *3D Printing of Highly Stretchable, Shape-Memory and Self-Healing Elastomer toward Novel 4D Printing.* ACS Applied Materials & Interfaces, 2018. **10**(8): p. 7381-7388.
28. Cesarano, T., T.A. Baer, and P. Calvert. *Recent developments in freeform fabrication of dense ceramics from slurry deposition*. in *1997 International Solid Freeform Fabrication Symposium*. 1996.
29. Alain, C., S. Emanuel, and C. Salvatore, *Design and fabrication of cast orthopedic implants with freeform surface textures from 3 - D printed ceramic shell.* Journal of Biomedical Materials Research, 2000. **53**(5): p. 525-535.
30. Ahn, B.Y., et al., *Planar and Three-Dimensional Printing of Conductive Inks.* Journal of Visualized Experiments : JoVE, 2011(58): p. 3189.
31. Quanyi, M., et al., *Thermal cure effects on electromechanical properties of conductive wires by direct ink write for 4D printing and soft machines.* Smart Materials and Structures, 2017. **26**(4): p. 045008.
32. Zhang, Q., et al., *Highly stretchable and conductive fibers enabled by liquid metal dip-coating.* Smart Materials and Structures, 2018. **27**(3): p. 035019.
33. Barry, R.A., et al., *Direct-Write Assembly of 3D Hydrogel Scaffolds for Guided Cell Growth.* Advanced Materials, 2009. **21**(23): p. 2407-2410.
34. Armstrong, C.D., et al., *A 3D Printed Morphing Nozzle to Control Fiber Orientation during Composite Additive Manufacturing.* Advanced Materials Technologies, 2020. **n/a**(n/a): p. 2000829.
35. Lewis, J.A., *Direct Ink Writing of 3D Functional Materials.* Advanced Functional Materials, 2006. **16**(17): p. 2193-2204.
36. Wu, A.S., et al., *3D Printed Silicones with Shape Memory.* Scientific Reports, 2017. **7**(1): p. 4664.
37. Ambulo, C.P., et al., *Four-dimensional Printing of Liquid Crystal Elastomers.* ACS Applied

Materials & Interfaces, 2017. **9**(42): p. 37332-37339.
38. Lu, X., et al., *4D-Printing of Photoswitchable Actuators.* Angewandte Chemie International Edition, 2020. **n/a**(n/a).
39. Kuang, X., et al., *Advances in 4D Printing: Materials and Applications.* Advanced Functional Materials, 2019. **29**(2): p. 1805290.
40. Caccese, V., J.R. Ferguson, and M. Edgecomb, *Optimal Design of Honeycomb Material Used to Mitigate Head Impact.* Compos Struct, 2013. **100**: p. 404-412.
41. Kuang, X., et al., *Grayscale digital light processing 3D printing for highly functionally graded materials.* Science Advances, 2019. **5**(5): p. eaav5790.
42. Karyappa, R., A. Ohno, and M. Hashimoto, *Immersion precipitation 3D printing (ip3DP).* Materials Horizons, 2019. **6**(9): p. 1834-1844.
43. Rice, M.C., E.M. Arruda, and M.D. Thouless, *The use of visco-elastic materials for the design of helmets and packaging.* Journal of the Mechanics and Physics of Solids, 2020. **141**: p. 103966.
44. Mills, N.J., et al., *Finite element micromechanics model of impact compression of closed-cell polymer foams.* International Journal of Solids and Structures, 2009. **46**(3): p. 677-697.
45. Jang, W.-Y., A.M. Kraynik, and S. Kyriakides, *On the microstructure of open-cell foams and its effect on elastic properties.* International Journal of Solids and Structures, 2008. **45**(7): p. 1845-1875.
46. Gaitanaros, S., S. Kyriakides, and A.M. Kraynik, *On the crushing of polydisperse foams.* European Journal of Mechanics - A/Solids, 2018. **67**: p. 243-253.
47. Hsu, Y.-C., C.-H. Yu, and M.J. Buehler, *Using Deep Learning to Predict Fracture Patterns in Crystalline Solids.* Matter, 2020. **3**(1): p. 197-211.
48. Narayan, V., et al., *Estimation of Hot Torsion Stress Strain Curves in Iron Alloys Using a Neural Network Analysis.* ISIJ International, 1999. **39**(10): p. 999-1005.
49. Peng, G.C., et al., *Multiscale Modeling Meets Machine Learning: What Can We Learn?* Archives of Computational Methods in Engineering, 2020: p. 1-21.
50. Shen, L., J. Wu, and W. Yang, *Multiscale Quantum Mechanics/Molecular Mechanics Simulations with Neural Networks.* Journal of Chemical Theory and Computation, 2016. **12**(10): p. 4934-4946.
51. Gu, G.X., S. Wettermark, and M.J. Buehler, *Algorithm-driven design of fracture resistant composite materials realized through additive manufacturing.* Additive Manufacturing, 2017. **17**: p. 47-54.
52. Jordan, B., M.B. Gorji, and D. Mohr, *Neural network model describing the temperature- and rate-dependent stress-strain response of polypropylene.* International Journal of Plasticity, 2020: p. 102811.
53. Hetzroni, A., et al., *Machine vision monitoring of plant health.* Advances in Space Research, 1994. **14**(11): p. 203-212.
54. Ye, X.W., C.Z. Dong, and T. Liu, *A Review of Machine Vision-Based Structural Health Monitoring: Methodologies and Applications.* Journal of Sensors, 2016. **2016**: p. 7103039.
55. Jafari Malekabadi, A., et al., *Development of a machine vision system for determination of mechanical properties of onions.* Computers and Electronics in Agriculture, 2017. **141**: p. 131-139.
56. Reu, P.L. and T.J. Miller, *The application of high-speed digital image correlation.* The Journal of Strain Analysis for Engineering Design, 2008. **43**(8): p. 673-688.

57. Landauer, A.K., et al., *A q-Factor-Based Digital Image Correlation Algorithm (qDIC) for Resolving Finite Deformations with Degenerate Speckle Patterns.* Experimental Mechanics, 2018. **58**(5): p. 815-830.
58. Landauer, A.K., et al., *Experimental characterization and hyperelastic constitutive modeling of open-cell elastomeric foams.* Journal of the Mechanics and Physics of Solids, 2019. **133**: p. 103701.
59. Zhai, X., et al., *Mechanical behaviors of auxetic polyurethane foam at quasi-static, intermediate and high strain rates.* International Journal of Impact Engineering, 2019. **129**: p. 112-118.
60. Niazi, A. and R. Leardi, *Genetic algorithms in chemometrics.* Journal of Chemometrics, 2012. **26**(6): p. 345-351.
61. Weile, D.S. and E. Michielssen, *Genetic algorithm optimization applied to electromagnetics: a review.* IEEE Transactions on Antennas and Propagation, 1997. **45**(3): p. 343-353.
62. Rohskopf, A., et al., *Empirical interatomic potentials optimized for phonon properties.* npj Computational Materials, 2017. **3**(1): p. 27.
63. Liu, B., et al., *Permutation genetic algorithm for stacking sequence design of composite laminates.* Computer Methods in Applied Mechanics and Engineering, 2000. **186**(2): p. 357-372.
64. Hamel, C.M., et al., *Machine-learning based design of active composite structures for 4D printing.* Smart Materials and Structures, 2019. **28**(6): p. 065005.
65. Wu, S., et al., *Evolutionary Algorithm-Guided Voxel-Encoding Printing of Functional Hard-Magnetic Soft Active Materials.* Advanced Intelligent Systems, 2020. **2**(8): p. 2000060.
66. Coley, D.A., *An Introduction to Genetic Algorithms for Scientists and Engineers*. An Introduction to Genetic Algorithms for Scientists and Engineers. 1999.
67. Bhoskar, M.T., et al., *Genetic Algorithm and its Applications to Mechanical Engineering: A Review.* Materials Today: Proceedings, 2015. **2**(4): p. 2624-2630.
68. Obayashi, S. *Multidisciplinary design optimization of aircraft wing planform based on evolutionary algorithms*. in *SMC'98 Conference Proceedings. 1998 IEEE International Conference on Systems, Man, and Cybernetics (Cat. No.98CH36218)*. 1998.
69. Cilla, M., et al., *Machine learning techniques for the optimization of joint replacements: Application to a short-stem hip implant.* PLOS ONE, 2017. **12**(9): p. e0183755.
70. Muc, A. and W. Gurba, *Genetic algorithms and finite element analysis in optimization of composite structures.* Composite Structures, 2001. **54**(2): p. 275-281.
71. Salonitis, K., D. Chantzis, and V. Kappatos, *A hybrid finite element analysis and evolutionary computation method for the design of lightweight lattice components with optimized strut diameter.* The International Journal of Advanced Manufacturing Technology, 2017. **90**(9): p. 2689-2701.
72. Reddy, S.K., D.B. Ferry, and A. Misra, *Highly compressible behavior of polymer mediated three-dimensional network of graphene foam.* RSC Advances, 2014. **4**(91): p. 50074-50080.
73. Petkovic, D., et al. *Verifying The Accuracy Of Machine Vision Algorithms And Systems*. in *Twenty-Second Asilomar Conference on Signals, Systems and Computers*. 1988.
74. Sharifi, M., M. Fathy, and M.T. Mahmoudi. *A classified and comparative study of edge detection algorithms*. in *Proceedings. International Conference on Information Technology: Coding and Computing*. 2002.
75. Kiryati, N., Y. Eldar, and A.M. Bruckstein, *A probabilistic Hough transform.* Pattern

Recognition, 1991. **24**(4): p. 303-316.

76. Hecht-Nielsen, R., *III.3 - Theory of the Backpropagation Neural Network**Based on "nonindent" by Robert Hecht-Nielsen, which appeared in Proceedings of the International Joint Conference on Neural Networks 1, 593–611, June 1989. © 1989 IEEE*, in *Neural Networks for Perception*, H. Wechsler, Editor. 1992, Academic Press. p. 65-93.

Supplemental Information

Utilizing Computer Vision and Artificial Intelligence Algorithms to Predict and Design the Mechanical Compression Response of Direct Ink Write 3D Printed Foam Replacement Structures

Devin J. Roach[1,4], Andrew Rohskopf [2], Craig M. Hamel [3],

William D. Reinholtz[4], Robert Bernstein[5], H. Jerry Qi[1*], Adam W. Cook [4*]

[1] The George W. Woodruff School of Mechanical Engineering, Georgia Institute of Technology, Atlanta, 30332 GA, USA

[2] Massachusetts Institute of Technology, Department of Mechanical Engineering, Cambridge, MA 02139, USA

[3] Materials and Failure Modeling, Sandia National Laboratories, 87123 NM, USA

[4] Advanced Materials Laboratory, Sandia National Laboratories, 87123 NM, USA

[5] Organic Materials Science, Sandia National Laboratories, 87123 NM, USA

[*] Corresponding authors: HJQ: qih@me.gatech.edu
AWC: acook@sandia.gov

S1. Multiple Mechanical Compression Cycle Hysteresis

As noted in the manuscript, only the first compression cycle was studied and used in the ANN. This is because subsequent compression cycles of the same foam result in a softening effect. Figure S1 shows the first three mechanical compression cycles observed in the experiments for FRS 51-53.

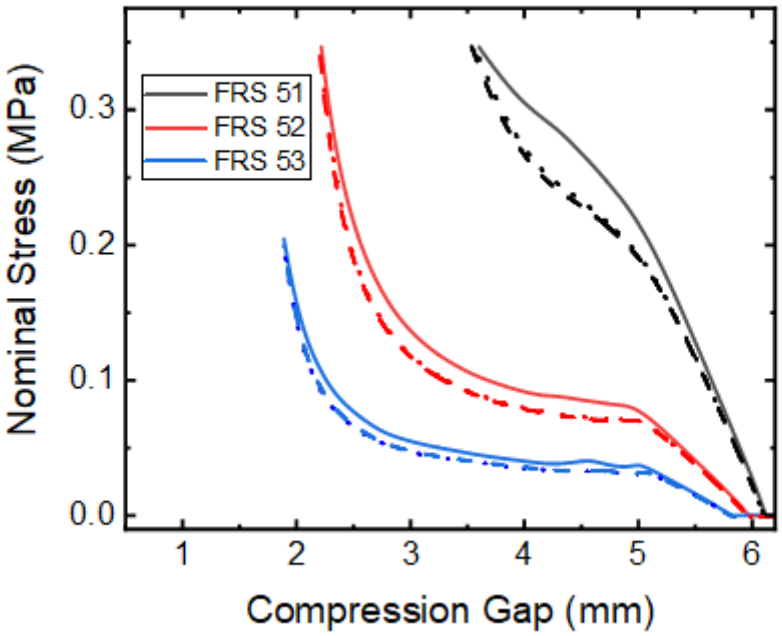

Figure S1: First three mechanical compression cycles for FRS 51-53 demonstrating a softening effect. The solid lines show the first compression cycle while the dotted lines show the second and third compression cycle.

S2. Images of DIW printed foams

Cross-sectional images of the DIW printed foam replacement structures (FRS) were obtained to be later used by the computer vision algorithm developed in this study. 250 total

cross-sectional images were taken and utilized. Figure S2 shows a sample of four FRS; FRS 2, FRS 17, FRS 51, and FRS 97. Their corresponding printing parameters are detailed below in Section S2.

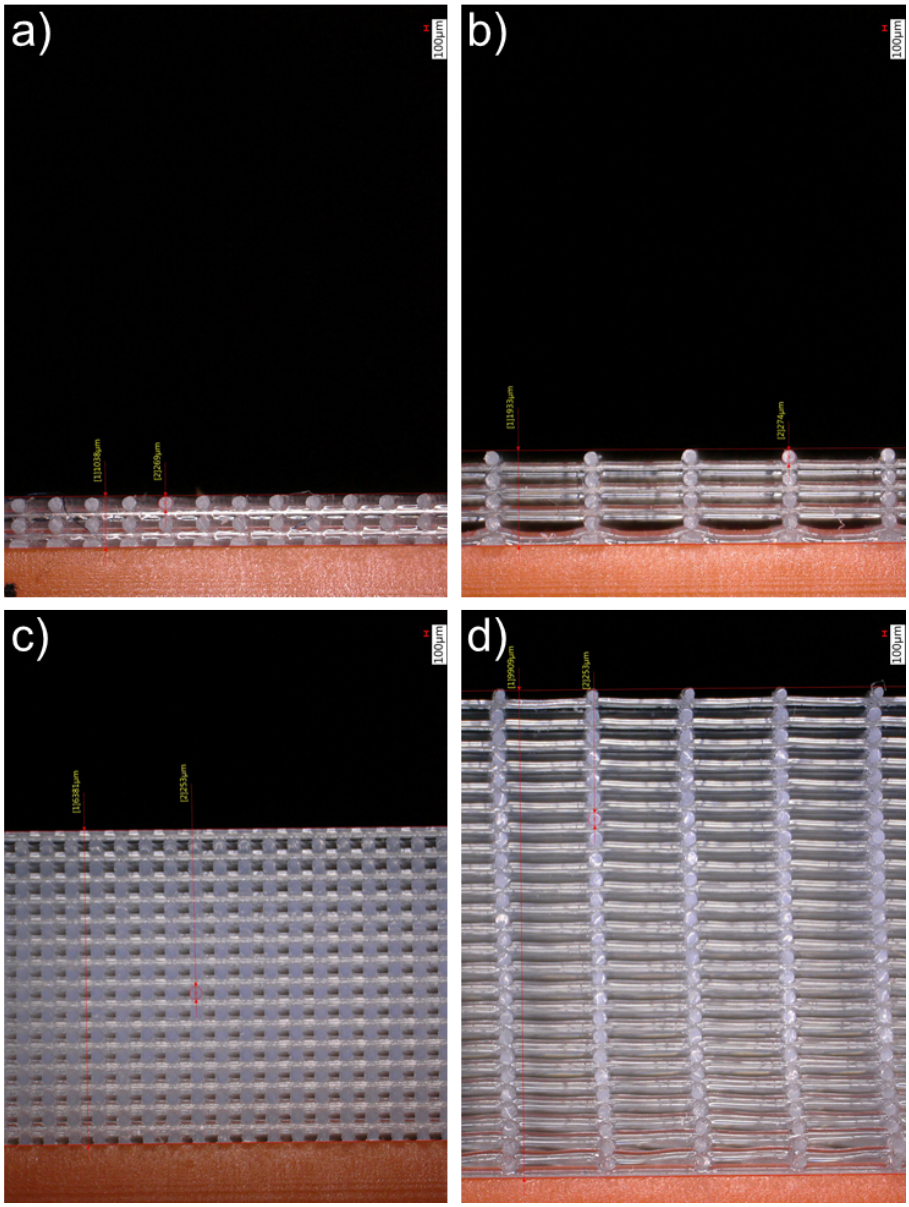

Figure S2: Images of some sample DIW printed FRS a) FRS 2, b) FRS 17, c) FRS 51, d) FRS 97.

S3. Tabulated foam printing parameters

Each of the 250 DIW printed FRS used in this study had unique printing parameters. Table S1 lists each of the DIW printing parameters and the corresponding FRS number as referenced within the figures and graphics in the article. It should be noted that the filament spacing is the number of filament diameters between each DIW printed line in the final FRS structure. A direct calculation of the filament spacing in millimeters can be determined by multiplying the filament diameter by the filament spacing number.

Table S1: DIW printing parameters and the corresponding FRS number for the design space explored in this experiment.

FRS Number	Filament Diameter (mm)	Layers	Filament Spacing
FRS 1	0.25	5	1
FRS 2	0.25	5	2
FRS 3	0.25	5	3
FRS 4	0.25	5	4
FRS 5	0.25	5	5
FRS 6	0.25	5	6
FRS 7	0.25	5	7
FRS 8	0.25	5	8
FRS 9	0.25	5	9
FRS 10	0.25	5	10
FRS 11	0.25	10	1
FRS 12	0.25	10	2
FRS 13	0.25	10	3
FRS 14	0.25	10	4
FRS 15	0.25	10	5
FRS 16	0.25	10	6
FRS 17	0.25	10	7
FRS 18	0.25	10	8
FRS 19	0.25	10	9
FRS 20	0.25	10	10
FRS 21	0.25	15	1
FRS 22	0.25	15	2
FRS 23	0.25	15	3
FRS 24	0.25	15	4
FRS 25	0.25	15	5
FRS 26	0.25	15	6
FRS 27	0.25	15	7

FRS 28	0.25	15	8
FRS 29	0.25	15	9
FRS 30	0.25	15	10
FRS 31	0.25	20	1
FRS 32	0.25	20	2
FRS 33	0.25	20	3
FRS 34	0.25	20	4
FRS 35	0.25	20	5
FRS 36	0.25	20	6
FRS 37	0.25	20	7
FRS 38	0.25	20	8
FRS 39	0.25	20	9
FRS 40	0.25	20	10
FRS 41	0.25	25	1
FRS 42	0.25	25	2
FRS 43	0.25	25	3
FRS 44	0.25	25	4
FRS 45	0.25	25	5
FRS 46	0.25	25	6
FRS 47	0.25	25	7
FRS 48	0.25	25	8
FRS 49	0.25	25	9
FRS 50	0.25	25	10
FRS 51	0.25	30	1
FRS 52	0.25	30	2
FRS 53	0.25	30	3
FRS 54	0.25	30	4
FRS 55	0.25	30	5
FRS 56	0.25	30	6
FRS 57	0.25	30	7
FRS 58	0.25	30	8
FRS 59	0.25	30	9
FRS 60	0.25	30	10
FRS 61	0.25	35	1
FRS 62	0.25	35	2
FRS 63	0.25	35	3
FRS 64	0.25	35	4
FRS 65	0.25	35	5
FRS 66	0.25	35	6
FRS 67	0.25	35	7
FRS 68	0.25	35	8
FRS 69	0.25	35	9
FRS 70	0.25	35	10

FRS 71	0.25	40	1
FRS 72	0.25	40	2
FRS 73	0.25	40	3
FRS 74	0.25	40	4
FRS 75	0.25	40	5
FRS 76	0.25	40	6
FRS 77	0.25	40	7
FRS 78	0.25	40	8
FRS 79	0.25	40	9
FRS 80	0.25	40	10
FRS 81	0.25	45	1
FRS 82	0.25	45	2
FRS 83	0.25	45	3
FRS 84	0.25	45	4
FRS 85	0.25	45	5
FRS 86	0.25	45	6
FRS 87	0.25	45	7
FRS 88	0.25	45	8
FRS 89	0.25	45	9
FRS 90	0.25	45	10
FRS 91	0.25	50	1
FRS 92	0.25	50	2
FRS 93	0.25	50	3
FRS 94	0.25	50	4
FRS 95	0.25	50	5
FRS 96	0.25	50	6
FRS 97	0.25	50	7
FRS 98	0.25	50	8
FRS 99	0.25	50	9
FRS 100	0.25	50	10
FRS 101	0.25	55	1
FRS 102	0.25	55	2
FRS 103	0.25	55	3
FRS 104	0.25	55	4
FRS 105	0.25	55	5
FRS 106	0.25	55	6
FRS 107	0.25	55	7
FRS 108	0.25	55	8
FRS 109	0.25	55	9
FRS 110	0.25	55	10
FRS 111	0.25	60	1
FRS 112	0.25	60	2
FRS 113	0.25	60	3

FRS 114	0.25	60	4
FRS 115	0.25	60	5
FRS 116	0.25	60	6
FRS 117	0.25	60	7
FRS 118	0.25	60	8
FRS 119	0.25	60	9
FRS 120	0.25	60	10
FRS 121	0.41	5	1
FRS 122	0.41	5	2
FRS 123	0.41	5	3
FRS 124	0.41	5	4
FRS 125	0.41	5	5
FRS 126	0.41	5	6
FRS 127	0.41	5	7
FRS 128	0.41	5	8
FRS 129	0.41	5	9
FRS 130	0.41	5	10
FRS 131	0.41	10	1
FRS 132	0.41	10	2
FRS 133	0.41	10	3
FRS 134	0.41	10	4
FRS 135	0.41	10	5
FRS 136	0.41	10	6
FRS 137	0.41	10	7
FRS 138	0.41	10	8
FRS 139	0.41	10	9
FRS 140	0.41	10	10
FRS 141	0.41	15	1
FRS 142	0.41	15	2
FRS 143	0.41	15	3
FRS 144	0.41	15	4
FRS 145	0.41	15	5
FRS 146	0.41	15	6
FRS 147	0.41	15	7
FRS 148	0.41	15	8
FRS 149	0.41	15	9
FRS 150	0.41	15	10
FRS 151	0.41	20	1
FRS 152	0.41	20	2
FRS 153	0.41	20	3
FRS 154	0.41	20	4
FRS 155	0.41	20	5
FRS 156	0.41	20	6

FRS 157	0.41	20	7
FRS 158	0.41	20	8
FRS 159	0.41	20	9
FRS 160	0.41	20	10
FRS 161	0.41	25	1
FRS 162	0.41	25	2
FRS 163	0.41	25	3
FRS 164	0.41	25	4
FRS 165	0.41	25	5
FRS 166	0.41	25	6
FRS 167	0.41	25	7
FRS 168	0.41	25	8
FRS 169	0.41	25	9
FRS 170	0.41	25	10
FRS 171	0.41	30	1
FRS 172	0.41	30	2
FRS 173	0.41	30	3
FRS 174	0.41	30	4
FRS 175	0.41	30	5
FRS 176	0.41	30	6
FRS 177	0.41	30	7
FRS 178	0.41	30	8
FRS 179	0.41	30	9
FRS 180	0.41	30	10
FRS 181	0.41	35	1
FRS 182	0.41	35	2
FRS 183	0.41	35	3
FRS 184	0.41	35	4
FRS 185	0.41	35	5
FRS 186	0.41	35	6
FRS 187	0.41	35	7
FRS 188	0.41	35	8
FRS 189	0.41	35	9
FRS 190	0.41	35	10
FRS 191	0.41	40	1
FRS 192	0.41	40	2
FRS 193	0.41	40	3
FRS 194	0.41	40	4
FRS 195	0.41	40	5
FRS 196	0.41	40	6
FRS 197	0.41	40	7
FRS 198	0.41	40	8
FRS 199	0.41	40	9

FRS 200	0.41	40	10
FRS 201	0.584	5	1
FRS 202	0.584	5	2
FRS 203	0.584	5	3
FRS 204	0.584	5	4
FRS 205	0.584	5	5
FRS 206	0.584	5	6
FRS 207	0.584	5	7
FRS 208	0.584	5	8
FRS 209	0.584	5	9
FRS 210	0.584	5	10
FRS 211	0.584	10	1
FRS 212	0.584	10	2
FRS 213	0.584	10	3
FRS 214	0.584	10	4
FRS 215	0.584	10	5
FRS 216	0.584	10	6
FRS 217	0.584	10	7
FRS 218	0.584	10	8
FRS 219	0.584	10	9
FRS 220	0.584	10	10
FRS 221	0.584	15	1
FRS 222	0.584	15	2
FRS 223	0.584	15	3
FRS 224	0.584	15	4
FRS 225	0.584	15	5
FRS 226	0.584	15	6
FRS 227	0.584	15	7
FRS 228	0.584	15	8
FRS 229	0.584	15	9
FRS 230	0.584	15	10
FRS 231	0.584	20	1
FRS 232	0.584	20	2
FRS 233	0.584	20	3
FRS 234	0.584	20	4
FRS 235	0.584	20	5
FRS 236	0.584	20	6
FRS 237	0.584	20	7
FRS 238	0.584	20	8
FRS 239	0.584	20	9
FRS 240	0.584	20	10
FRS 241	0.584	25	1
FRS 242	0.584	25	2

FRS 243	0.584	25	3
FRS 244	0.584	25	4
FRS 245	0.584	25	5
FRS 246	0.584	25	6
FRS 247	0.584	25	7
FRS 248	0.584	25	8
FRS 249	0.584	25	9
FRS 250	0.584	25	10

S4. Artificial Neural Network (ANN) Results

The experimental compression data was used to train the ANN with an 80, 10, 10 percent split between training, validation, and testing, respectively. For each epoch, or iteration, the ANN attempts to confirm the learned relationship between the inputs and outputs by validating the data. Here, we selected the ANN to finish training when a relationship with a low enough MSE is achieved for 6 different validation checks. Figure S3a shows the results of the ANN gradient descent as well as a graph depicting the validation attempts. Here, the ANN is attempting to validate the accuracy of the trained neural network using some of the validation data. The number of successful validation checks per epoch are shown with red diamonds demonstrating that when the threshold of six successful validations were achieved, the algorithm was successfully trained. Figure S3b shows that the ANN is sufficiently trained when the training data MSE reaches a minimum designated value of 0.1. Figure S3c demonstrates that the first x value that the neural network exports corresponds with the foam printed height, or the first value in the experimental compression curve.

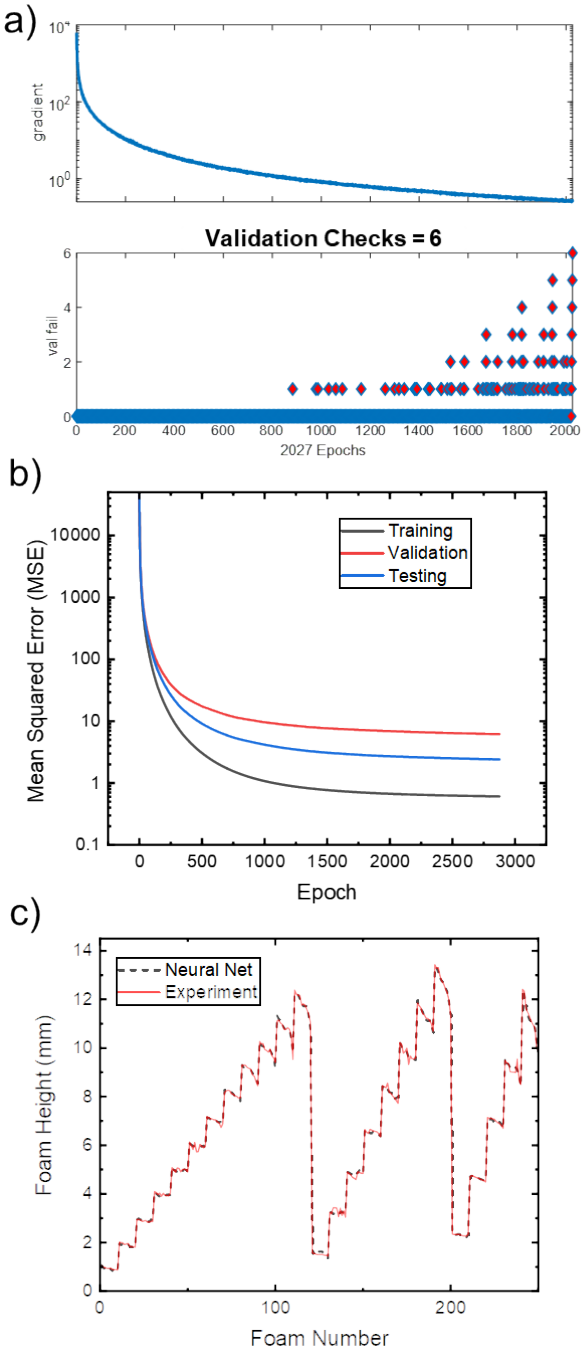

Figure S3: ANN training results. a) A rapidly decreasing error gradient as a function of training iterations as well as an increasing number of successful validation checks. b) Neural network convergence where the mean square error reaches a minimum after 2870 epochs. c) First x value output by the neural network vs. the first x value of the experimental compression curve. This first x value corresponds with the DIW printed FRS's height value.